Meltwater transport and mixing layer growth near the ice–ocean interface

Sofía Allende[1]†, Louis-Alexandre Couston[2], Simon Thalabard[3], and Benjamin Favier [1]

[1]Aix Marseille Univ, CNRS, Centrale Med, IRPHE, Marseille, France.

[2]Université Claude Bernard Lyon 1, ENS de Lyon, CNRS, LPENSL, UMR5672, Lyon, France.

[3]Université Côte d'Azur, CNRS, Institut de Physique de Nice, Nice, France.

(Received xx; revised xx; accepted xx)

Ice melting into saline water plays a fundamental role in the dynamics near the ice-ocean interface in polar oceans. The physics of meltwater transport involves a non-trivial interplay between thermodynamics at the interface, hydrodynamic transport in the bulk and the properties of the ambient ocean. The key control parameters are the density ratio R_ρ, which is proportional to the ambient salinity and measures the balance between the temperature and salinity effects on density, together with the Lewis number $Le = \kappa_T/\kappa_S$, which compares thermal and solutal diffusivities. In quiescent horizontal configurations, increasing the salinity is known to slow down melting, with the melt rate transitioning from subdiffusive to diffusive as R_ρ increases. Here, we assess the role of turbulence in this transition, using highly-resolved numerical simulations of the two-dimensional Boussinesq equations with a slowly melting upper boundary. We analyse the non-stationary growth of the thermal and solutal mixing layers, varying the Lewis number and the density ratio. While meltwater transport is continuously driven by convection within the bulk, we identify a transition from convection to diffusion close to the interface. This transition is reflected by the formation of an interfacial boundary layer that regulates the flux of meltwater pouring into the turbulent bulk. The boundary layer has little effect on thermal transport, but strongly suppresses solutal transport for $R_\rho \gtrsim 10$, only allowing a fraction $\propto R_\rho^{-1}$ of the input flux to reach the bulk. Using mixing-layer diagnostics based on solutal-concentration thresholds, we observe that the turbulent layer grows super-diffusively $\propto t^{1.33}$, while the interfacial boundary layer expands diffusively $\propto t^{0.5}$ but with a non-universal prefactor depending on Lewis and density ratio. The superdiffusive growth of the mixing layer challenges the commonly assumed picture of a fully diffusive regime at high salinity. Overall, our results indicate that double-diffusive effects are here confined to the interface, and highlight potential limitations of diagnostics based on fixed concentration thresholds in oceanographic applications.

1. Introduction

The melting of ice into salty water is a fundamental process that occurs in various natural environments, controlling the fate of polar ice shelves, sea ice, and glacial meltwater

† Email address for correspondence: sofia.allende@univ-amu.fr

plumes (Hewitt 2020; Du *et al.* 2024; Rosevear *et al.* 2025). Understanding its process is critical for predicting sea level rise and climate feedback mechanisms, as melting affects both local stratification and the transport of freshwater into the ocean (Jenkins 1999). Recent studies have emphasised the sensitivity of melting rates to thermodynamics at the interface (Keitzl *et al.* 2016), examined fluid instabilities caused by basal diffusion (Berhanu *et al.* 2021; Cohen *et al.* 2020), explored the role of turbulent mixing in influencing the properties of near-ice water (Couston 2024), and investigated the asymmetries between melting and freezing within convective systems (Yang *et al.* 2025).

The recent numerical studies by Xue *et al.* (2024) and Guo & Yang (2025), employing phase-field methods, suggest that in the absence of external flow, the interface dynamics is controlled by the density ratio R_ρ a non-dimensional number later defined in Eq. (2.6), which is proportional to ambient ocean salinity and reflects the balance between the temperature and salinity effects on density. Over relatively fresh ambient water (small R_ρ), mixing is dominated by thermal convection, and ice melts relatively rapidly in time, following a sub-diffusive scaling $\propto t^{-r}$ with the exponent $r \lesssim 0.2$. Over relatively salty ambient water (large R_ρ), the system instead develops a strongly stratified, diffusion-dominated regime, with the melt rate exhibiting a diffusive scaling $\propto t^{-0.5}$, as also reported by Middleton *et al.* (2021).

Here, we revisit the turbulence generated by a block of freshwater ice immersed in initially quiescent, warm, salty ocean water. In Xue *et al.* (2024) and Guo & Yang (2025), the physics of the melting interface is treated in considerable detail, making nonlinear effects away from the interface difficult to isolate. Our setting explores the opposite limit: a simplified modeling of the interface, allowing nonlinear effects away from it to be more clearly assessed. Our study focuses on the early-time growth of the mixing layer (*i.e.*, while unaffected by the bottom boundary) and its connection to the melt rate at the ice–ocean interface. We use high-resolution numerical simulations of the Boussinesq system under a linearised equation of state, inside a vertically bounded and horizontally periodic two-dimensional domain—supplemented by a slowly melting condition at the top boundary. We investigate how the Lewis number (the ratio of thermal to saline diffusivity) and the density ratio impact the dynamics.

In our configuration, a convective mixing layer develops, which grows super-diffusively $\propto t^{1.33}$ and self-similarly in time. The growth rate is largely universal, as it does not depend on double diffusive effects, which are absent in the bulk, nor on the melt rate at the top boundary. Over sufficiently saline environments, we recover the formation of a meltwater boundary layer, which produces a diffusive regime of melting. The interfacial layer does not suppress the turbulence inside the convective mixing layer, nor does it significantly modify its statistics. However, it regulates the amount of meltwater poured into the bulk: we find that the ratio between the convective and diffusive contributions to the solutal fluxes decreases at a rate $\propto (LeR_\rho)^{-1}$, depending both on the Lewis and the density ratio. Because of its relative simplicity, our setting allows for some theoretical understanding of the meltwater transport, from the diffusive to the convective stages.

The paper is organized as follows: §2 describes the physical and numerical setup, §3 presents the main results, contrasting interface and bulk dynamics and discussing mixing length definitions. Finally in §4, we share some concluding remarks. Additional technical details related to numerical setups and theoretical arguments are described in Appendix.

2. Numerical set-up

We consider the flow illustrated in Fig. 1, which is initially quiescent. The domain is two-dimensional (2D), with horizontal extent L_x and depth $L_z = L_x$. The initial salinity S is uniform and equal to the far-field value S_∞, while the temperature T has a step-profile

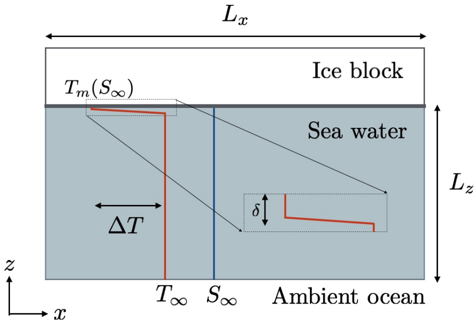

Figure 1: Initial configuration

Heat capacity of seawater	C_p	$3974\ JK^{-1}kg^{-1}$
Latent heat	L_f	$3.35 \times 10^5 Jkg^{-1}$
Freezing slope	λ_1	$-5.73 \times 10^{-2}\ K(g/kg)^{-1}$
Thermal expansion	β_T	$3.87 \times 10^{-5}\ K^{-1}$
Haline contraction	β_S	$7.86 \times 10^{-4}\ (g/kg)^{-1}$
Temperature jump	ΔT	$2\ K$
Freezing point of pure water	$T_{f,0}$	$273.15\ K$
Kinematic viscosity	ν	$1.8 \times 10^{-6}\ m^2s^{-1}$
Thermal diffusivity	κ_T	$1.8 \times 10^{-6}\ m^2s^{-1}$
Gravitational acceleration	g	$9.8\ ms^{-2}$
Depth	L_z	$6.28\ m$
Horizontal extent	L_x	$6.28\ m$

Table 1: Physical parameters

characterized by a temperature jump $\Delta T = T_\infty - T_m(S_\infty)$. This represents the difference between the far-field temperature T_∞ and the melting temperature $T_m(S_\infty) = T_{f,0} + \lambda_1 S_\infty$.

We later work with non-dimensional variables for temperature and salinity, defined as

$$\begin{gathered} \theta = \frac{T - T_\infty}{\Delta T} \quad \text{and} \quad \sigma = \frac{S - S_\infty}{\Delta S} \\ \text{where} \quad \Delta T := T_\infty - T_m(S_\infty), \quad \Delta S := \frac{\beta_T}{\beta_S}\Delta T. \end{gathered} \tag{2.1}$$

Here, ΔS is the salinity variation required to compensate the density change caused by ΔT, according to the linearised equation of state

$$\rho = \rho_0 \left[1 - \beta_T T + \beta_S S\right], \tag{2.2}$$

which we adopt here for simplicity. We model the fluid dynamics with the two-dimensional incompressible Navier-Stokes equations under the Boussinesq approximation.

Defining the horizontal length L_x, the velocity $U_0 := \sqrt{2g\beta_T \Delta T L_x}$, and the time $t_0 = L_x/U_0$, as characteristic scales, the equations of motion take the dimensionless form

$$\begin{gathered} \partial_t \mathbf{u} + (\mathbf{u}\cdot\nabla)\mathbf{u} + \nabla p = Re^{-1}\Delta\mathbf{u} + \mathbf{e_z}\frac{\theta - \sigma}{2}, \qquad \nabla\cdot\mathbf{u} = 0, \\ \partial_t\theta + (\mathbf{u}\cdot\nabla)\theta = Re^{-1}\,Pr^{-1}\Delta\theta, \\ \partial_t\sigma + (\mathbf{u}\cdot\nabla)\sigma = Re^{-1}\,Pr^{-1}\,Le^{-1}\Delta\sigma, \end{gathered} \tag{2.3}$$

with non-dimensional parameters

$$Re = \frac{U_0 L_x}{\nu}\text{(Reynolds)}, \quad Pr = \frac{\nu}{\kappa_T}\ \text{(Prandtl)} \quad \text{and} \quad Le = \frac{\kappa_T}{\kappa_S}\ \text{(Lewis)}. \tag{2.4}$$

The Prandtl and the Lewis numbers represent the ratio of viscosity to thermal diffusivity and thermal to salt diffusivity, respectively.

The boundary conditions represent a (no-slip) melting ice–ocean interface at the top coupled to a far-field quiescent state at the bottom, similar to Couston (2024). At the top boundary, the temperature θ is set equal to the local melting temperature, which depends linearly on salinity. This condition is supplemented by a balance between heat and haline fluxes, which determine the melt rate following the widely adopted Stefan condition (Middleton *et al.* 2021; Vreugdenhil & Taylor 2019; Gayen *et al.* 2016). The conditions read in dimensionless form

$$\begin{cases} z = 0 \quad \text{(melting)}: \;\; \theta = -1 - \gamma_1 \sigma \quad \text{and} \quad \dfrac{\partial_z \sigma}{(\sigma + R_\rho)} = Le St \partial_z \theta \\ z = -1 \quad \text{(far field)}: \quad \theta = 0 \quad \text{and} \quad \sigma = 0, \end{cases} \tag{2.5}$$

with

$$R_\rho = \frac{S_\infty}{\Delta S} \text{ (density ratio)}, \;\; \gamma_1 = -\lambda_1 \frac{\beta_T}{\beta_S} \text{ (freezing coupling)}, \; St = \frac{C_p}{L_f} \Delta T \text{ (Stefan)}. \tag{2.6}$$

The density ratio R_ρ quantifies the balance between the stabilising effect of the far-field salinity and the destabilising temperature difference. The parameter γ_1 represents a freezing coefficient coupling temperature and salt at the meting interface; the Stefan number St characterises the relative importance of specific and latent heat, based on the initial temperature jump at the interface. These boundary conditions are approximations that hold true only when the melting rate is slow. Essentially, they substitute the mass flux resulting from the phase change with a diffusive flux, introducing a Lewis dependence in Eq. (2.5). This approach serves as an alternative to directly solving the Stefan problem, which, strictly speaking, requires explicit treatment of a moving interface—see, *e.g.*, (Huppert 1990; Wettlaufer 2001). While phase-field methods can be employed to this end, they prove computationally expensive for small melting rates, which produce a large time-scale separation between the dynamics of phase change and that of the fluid (Favier *et al.* 2019; Gastine & Favier 2025).

Our numerical setup employs direct numerical simulations using the finite-volume code Oceananigans (Ramadhan *et al.* 2020). The computational domain is discretised on a grid of 8192^2 collocation points, uniform in the horizontal direction and refined vertically near the top interface. For this resolution, the spectra of the scalar fields exhibits a clear decay at high wavenumbers (not shown), indicating that the smallest dynamically active scales are adequately resolved by the numerical grid. Since Oceananigans operates with dimensional variables, all governing parameters are prescribed in physical units, for consistency with realistic seawater properties (Couston 2024; Allende *et al.* 2024). They are summarised in Table 1, and prescribe the free-fall velocity and time units as $U_0 \approx 0.098\, m/s$ and $t_0 \approx 64 s$, respectively.

In all the simulations, we set $\Delta T = 2\mathrm{K}$. To explicity satisfy the boundary conditions (2.5), we regularise the initial temperature jump by introducing a smooth temperature profile controlled by the (small) parameter $\delta \ll L_x$—see Fig.1. The parameter δ sets the initial gradient $\propto \Delta T/\delta$, and offsets it down from the upper boundary, at a depth $\propto \delta$. This smoothing ensures that the temperature gradient vanishes at the top boundary, hence fulfilling the boundary condition (2.5) imposed by the uniform salinity profile. To trigger the instability, the initial temperature profile of Fig. 1 is perturbed by a random noise of small amplitude—see Appendix A for additional details. Our series of simulations vary the Lewis number from 1 to 100, keeping the thermal diffusivity constant. The density ratio R_ρ varies from 1 to 406, tracking modifications in S_∞. The parameters in Table 1 additionally prescribe the non-dimensional values: $Pr = 1$, $St = 2.4 \times 10^{-2}$ and $\gamma_1 = 2.8 \times 10^{-3}$, representative of polar ice–ocean conditions, though slightly idealised for numerical efficiency—in particular $Pr = O(10)$ in seawater. Additional simulations at $Pr = 7$ (not shown) display similar flow behaviours.

From an oceanographic perspective, please note that $R_\rho = O(10)$ corresponds to weakly saline conditions ($S_\infty \sim 1 g/kg$), which are representative of near-surface environments influenced by strong freshwater inputs. By contrast, values $R_\rho \gtrsim 300$ corresponds to typical open-ocean salinities $S_\infty \gtrsim 30 g/kg$ encountered in polar oceans (Peralta-Ferriz & Woodgate

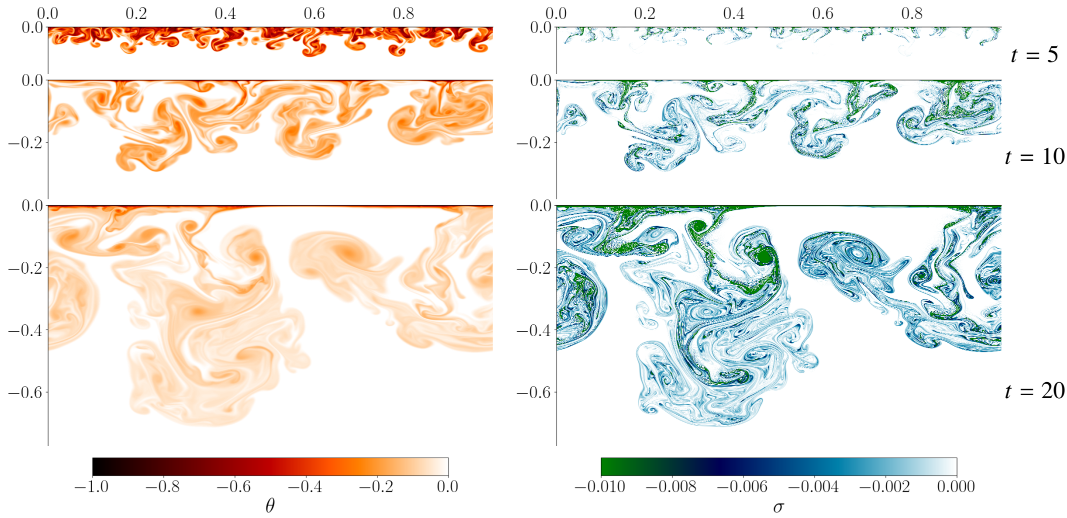

Figure 2: Typical evolution of the temperature (left) and salinity fields (right) for a simulation with $Le = 100$ and $R_\rho = 406$.

2015). For these values, the linearised equation of state (2.2) predicts that the density decreases monotonically with the temperature and this is consistent with the observations—see, *e.g.*, (Millero 2010; Talley 2011). While the linearised equation of state is less accurate at lower salinities, it still provides a well-defined hydrodynamical framework, allowing for a systematic investigation of nonlinear melting dynamics and their sensitivity to key control parameters. In the present study, we therefore deliberately adopt a linear equation of state to retain a tractable framework and isolate the dominant physical mechanisms. The effects of a nonlinear equation of state, including the freshwater density anomaly, have been investigated in recent studies (e.g. Yang *et al.* (2023); Xu *et al.* (2025)) and are beyond the scope of the present work.

3. Results

In all simulations, the fluid evolves through three main phases. This is illustrated in Fig. 2, showing representative temperature and salinity snapshots. The system initially develops a Rayleigh–Taylor-like instability, which arises from the initially unstable buoyancy jump away from the interface (Drazin & Reid 2004; Boffetta & Mazzino 2017). This is followed by the interaction of the flow with the upper boundary and the onset of melting. Eventually, a mixing layer develops near the upper boundary and gradually deepens, with cold and fresh plumes extending downward into the domain. Note that contrary to previous studies with similar configurations (Guo & Yang 2025), we here focus on the transient dynamics before the turbulent layer reaches the bottom of the numerical domain and will not comment on the subsequent stationary (or quasi-stationary) states. Varying Le and R_ρ, the main difference is seen not in the bulk but at the melting interface. Increasing R_ρ, the top interfacial layer of fresh water gets thicker, as seen from the horizontally-averaged salinity profiles in Fig. 3. No obvious difference is seen for the temperature, neither in the bulk nor at the interface. These observations suggests the following phenomenology: Salty environments favour strong stratification between the relatively fresh meltwater layer and the ambient ocean leading to a stable diffusive layer, while low density ratios favour mixing close to the upper interface.

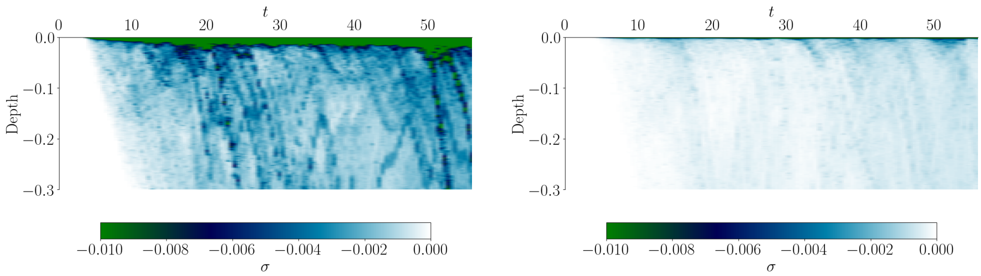

Figure 3: Left: Temporal evolution of the horizontally-averaged salinity profile for $Le = 100$ and $R_\rho = 406$. Right: Same but for for $Le = 100$ and $R_\rho = 1$.

3.1. *Fluxes and temperature at the top interface*

To quantify the melt-rate, we introduce the Nusselt number,

$$Nu = -\langle \partial_z \theta \rangle_{z=0}\,, \tag{3.1}$$

with $\langle \cdot \rangle$ denoting horizontal averaging. Analogous to Rayleigh–Bénard (RB) convection, the Nusselt number measures the thermal flux at the top boundary in units of the average temperature gradient $\Delta T / L_x$—recall that $L_x = 1$ in our length units. It is directly proportional to the melt rate, $Nu \propto Le\, St\, \partial_z \theta|_{z=0}$. With the conventional minus sign in (3.1), the regime $Nu > 0$ reflects melting (this is the case under study) while $Nu < 0$ would indicate freezing. Unlike RB convection, Nu decays over time. Its algebraic rate of decay exhibits two distinct asymptotic regimes, highlighting a strong dependence on the density ratio R_ρ and only a weak dependence on Le—see Fig. 4. In fresh environments, *i.e*, for small values of $R_\rho \lesssim 10$, the Nusselt number decays only mildly as $Nu \sim C_f t^{-0.2}$, where both the exponent and the prefactor are insensitive to the Lewis number. In salty environments, *i.e*, for large values of $R_\rho \gtrsim 10$, we observe a diffusive scaling $Nu \sim C_s t^{-0.5}$, with the prefactor following the apparent scaling law $C_s \sim Le^a R_\rho^b$. Our simulations indicate $a \simeq 0.1$ and $b \simeq -0.3$, meaning that the Lewis and density ratio have opposite effects, respectively enhancing and slowing melting in this apparent diffusive regime.

The salinity at the boundary modifies the freezing temperature at the interface. Fig. 5 shows the evolution with time of the excess temperature (*i.e.*, above the freezing temperature based on the far-field salinity)

$$\theta_0 := 1 + \langle \theta \rangle_{x,z=0} = -\gamma_1 \sigma_0, \tag{3.2}$$

where $\sigma_0 = \langle \sigma \rangle_{x,z=0}$. The second equality indicates that θ_0 is proportional to the horizontally averaged fluctuation in salinity—see Eq.(2.5). Positive flučtations $\theta_0 \geqslant 0$ are associated with fresh water at the interface, $\sigma_0 \leqslant 0$. Unlike the Nusselt number, no clear dichotomy emerges. In all the simulations, the top temperature quickly reaches a quasi-stationary value, yielding the scaling behavior $\theta_0 \propto Le^{0.5} R_\rho$. Theoretically, this scaling reflects a diffusive dynamics near the melting boundary—see Appendix B. It is consistent with the intuitive idea that saltier ambient water favors a comparatively fresher interfacial boundary layer near the top interface.

3.2. *Meltwater transport: from diffusion to convection*

Our setup employs a regularization that offsets the initial temperature jump between the ice and the underlying bulk fluid by a depth $\delta \ll 1$. This triggers a classical Rayleigh–Taylor turbulent mixing layer. Without an upper boundary, the layer would grow quadratically

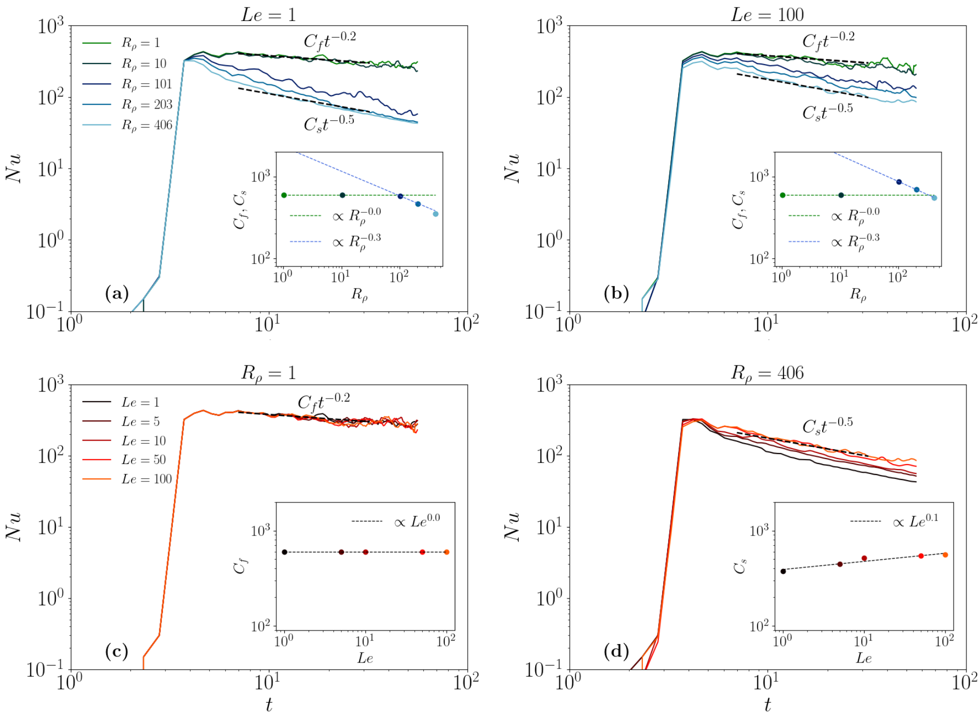

Figure 4: Time evolution of the Nusselt number Nu, varying R_ρ for fixed Le (top) and Le for fixed R_ρ (bottom). In all four panels, the insets display the prefactors C_s, C_f (see text) averaging over times $t \gtrsim 10$.

$L(t) \sim t^2$ under a critical balance between buoyancy and nonlinear terms—this is the self-similar Bolgiano–Obukhov scenario (Chertkov 2003; Boffetta & Mazzino 2017). The interaction with the top interface, however, disrupts this classical regime by creating a (meltwater) boundary layer that couples the melting interface to the turbulent mixing layer. To characterise the exchange between the boundary layer and the turbulent layer, we examine the vertical fluxes of temperature and salinity. After horizontal averaging, each flux can be decomposed into convective and diffusive contributions as

$$\phi_\chi = \phi_\chi^c + \phi_\chi^d, \quad \phi_\chi^c = \langle \chi u_z \rangle, \quad \phi_\chi^d = -\lambda_\chi^{-1} Pr^{-1} Re^{-1} \langle \partial_z \chi \rangle, \quad \chi \equiv \theta, \sigma \tag{3.3}$$

with $\lambda_\theta = 1$ and $\lambda_\sigma = Le$. Figure 6 illustrates the generic behaviour using the most saline environment $R_\rho = 406$ at $Le = 100$, highlighting two propagation rates. At any time during the growth, the convective fluxes $\phi_\theta^c, \phi_\sigma^c$ fluctuate in z about a nearly constant value before dropping sharply. These drops become synchronised from $t \gtrsim 2$, defining the extent of the convective mixing layer. The layer propagates superdiffusively and reaches the bottom interface at $t \simeq 27$ as

$$L(t) \simeq C\, t^\beta, \quad C \approx 0.015, \quad \beta \simeq 1.33. \tag{3.4}$$

The diffusive contributions $\phi_\theta^d, \phi_\sigma^d$ evolve on slower timescales, following the (diffusive) scalings

$$\delta_\chi(t) = \lambda_\chi^{-1/2} Re^{-1/2} Pr^{-1/2} t^{1/2}, \quad \chi \equiv \theta, \sigma \tag{3.5}$$

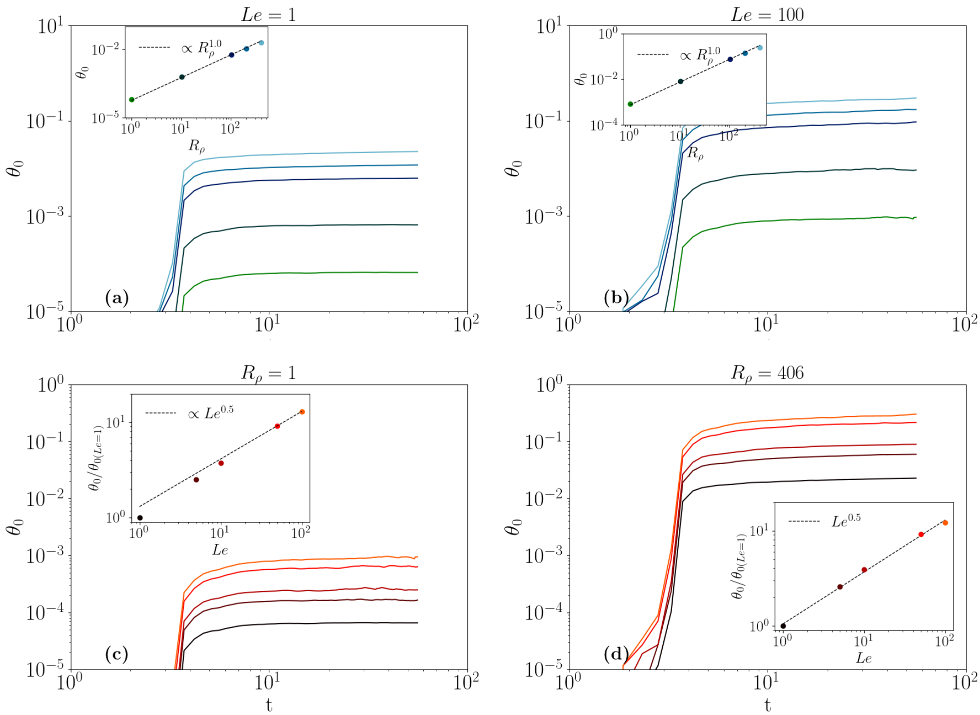

Figure 5: Time evolution of the excess temperature θ_0, varying R_ρ at fixed Le (top) and Le at fixed R_ρ (bottom). In all four panels, the insets display the dependence on either R_ρ or Le averaging over times $t \gtrsim 10$.

see Appendix A. In Fig. 6, this differential propagation is signaled by the collapse of the convective and diffusive fluxes shown in the panels c,d,e and f. These collapses are obtained by rescaling lengths with the superdiffusive scaling (3.4) and the diffusive scaling (3.5), respectively. At each time, the crossovers between diffusive and convective contributions define the effective boundary layer thicknesses $\propto \delta_\theta, \delta_\sigma$ for the solutal and thermal field, respectively. Within this layer, the transport of meltwater is diffusive and hence sensitive to double-diffusive effects. Below this layer, solutal and thermal transport is convective, but in a non-trivial way. While this convection originates from the nonlinear stages of the initial RT instability, it does not propagate following the critical-balance scaling $\propto t^2$. Instead, the superdiffusive rate (3.4) reflects the presence of a boundary at $z = 0$.

3.3. *Constant-in-space heat flux scenario for the superdiffusive growth* $\propto t^{4/3}$

The collapse in Fig. 6 with the superdiffusive rates (3.4) suggests a constant-flux propagation scenario through the domain. This can arise if the convective thermal and solutal fluxes evolve self-similarly as

$$\phi^c_\chi(z,t) \sim L^{-\alpha}\Phi_\chi\left(\frac{|z|}{L(t)}\right) + \text{fluctuations}, \qquad \chi \equiv \theta, \sigma, \tag{3.6}$$

involving similarity flux profiles Φ_θ, Φ_σ. The exponent α prescribes the decay rate $\propto (|z|/L)^{-\alpha}$ of the convective flux across the mixing layer. For example, setting $\alpha = 0$ gives a scenario where the convective fluxes are approximately uniform across the mixing layer. Regardless of the exponent, the horizontally averaged fields must also be self-similar within

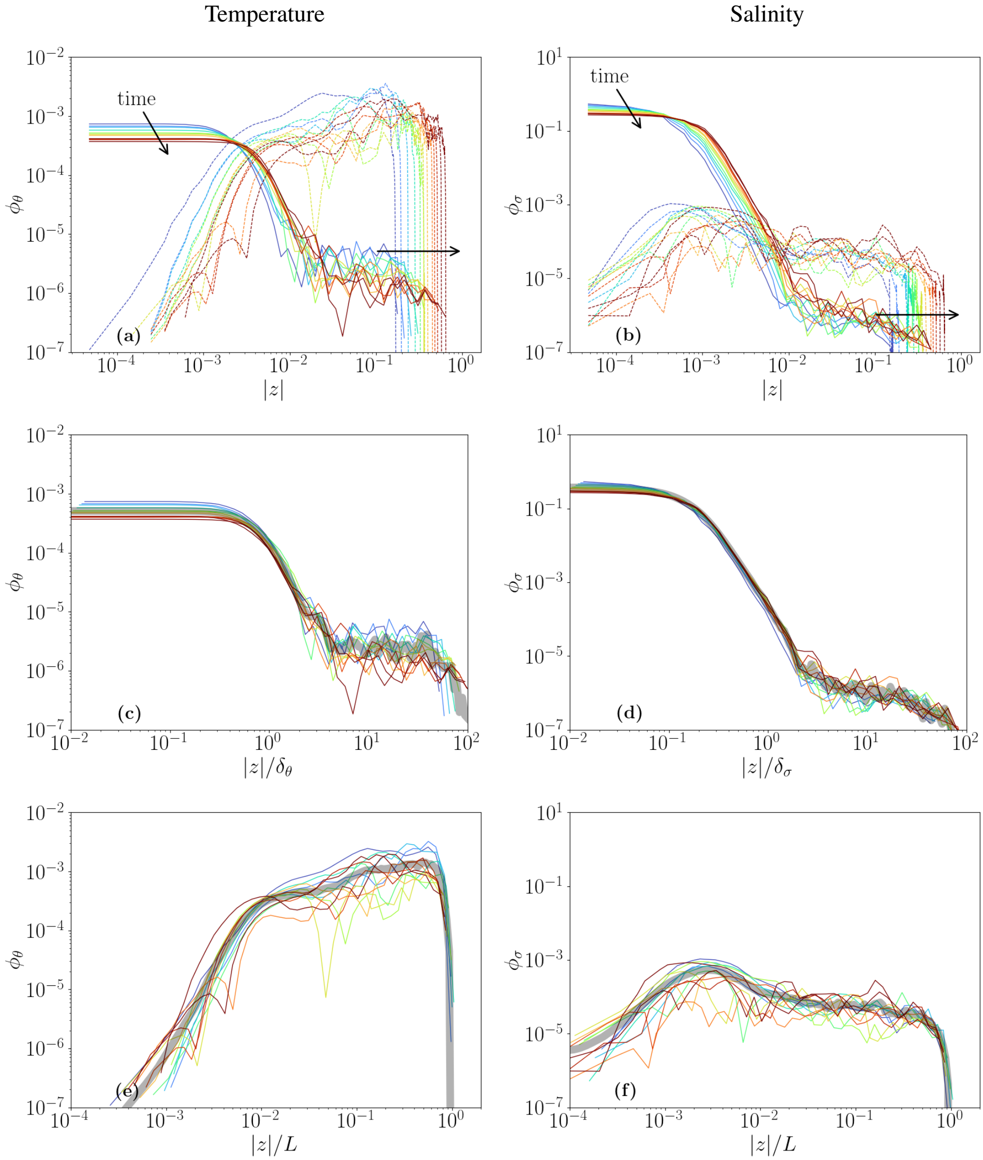

Figure 6: Top: Vertical fluxes at successive times for the case $Le = 100$ and $R_\rho = 406$, decomposed into their diffusive (solid lines) or convective (dashed lines) contributions. Middle: Diffusive contributions rescaled using the diffusive scaling $\delta_\chi(t) \propto t^{1/2}$. Bottom: Convective contributions rescaled using the superdiffusive scaling $L(t) \propto t^{4/3}$. Panels (a,c,e) are for the thermal fluxes. Panels (b,d,f) are for the solutal fluxes.

the mixing layer,

$$\langle \theta \rangle (z,t) \sim L^{-x}\Theta\left(\frac{|z|}{L(t)}\right) + \text{fluctuations}, \quad \langle \sigma \rangle (z,t) \sim L^{-x}\Sigma\left(\frac{|z|}{L(t)}\right) + \text{fluctuations}, \tag{3.7}$$

for some exponent $x \geqslant 0$. This form implies the algebraic behavior $\propto (|z|/L)^{-x}$ far away from the front but within the mixing layer, *i.e.* $\delta_\theta, \delta_\sigma \ll |z| \ll L$—see, *e.g.*, (Barenblatt

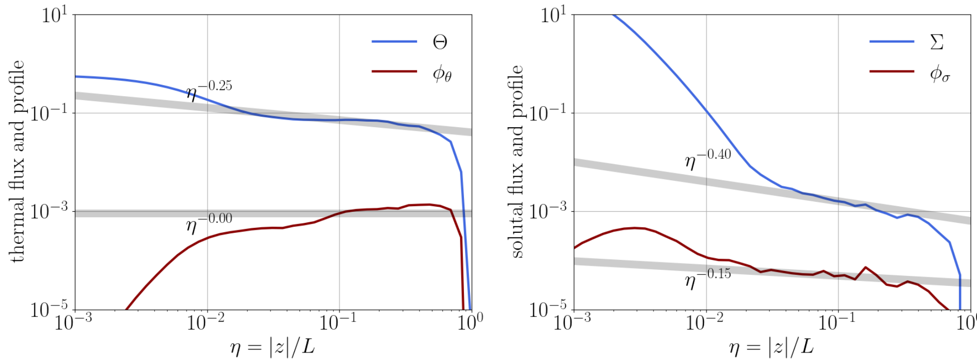

Figure 7: Similarity profiles obtained from the scalar fields and fluxes for $Le = 100$ and $R_\rho = 406$. Left: Temperature, with the exponents $\alpha = 0, x = 0.25$. Right: Salinity with the exponents $\alpha = 0.15, x = 0.4$.

1996; Campolina *et al.* 2025). In turn, this prescribes the behaviors for the similarity profiles

$$\Phi_\chi(\eta) \sim |\eta|^{-\alpha}, \quad \Sigma(\eta),\ \Theta(\eta) \sim |\eta|^{-x} \quad |\eta| \ll 1. \tag{3.8}$$

Assuming an algebraic growth $L \propto t^\beta$, the dimensional balance between the transport terms $\partial_z \phi_\theta^c$ and $\partial_t \langle\theta\rangle$ prescribes that the three exponents β, x, α satisfy

$$\beta(1 + \alpha - x) = 1 \tag{3.9}$$

Provided that $x < 1$, then the temperature field evolves as

$$\frac{d}{dt}\int_{-\infty}^{0} dz\ \theta(z,t) = \begin{cases} (PrRe)^{-1} Nu(t) \\ \beta(1-x)t^{\beta-\beta x-1} \displaystyle\int_0^1 \Theta(\eta) d\eta \propto t^{-\alpha\beta} \end{cases}; \tag{3.10}$$

where the first and second lines in the rhs are obtained from the boundary flux and from the self-similar scaling, respectively.

Combined with the growth exponent $\beta = 1.33$ from Eq. (3.4), the compatibility Eq. (3.9) prescribes in particular $x - \alpha \simeq 0.25$ leaving only one exponent to be determined, say α. In turn, Eq. (3.10) relates the exponent α to the decay of Nusselt. The Nusselt decay $Nu \propto t^{-0.2}$ reported in Fig. 4 suggest $\alpha\beta \simeq 0.2$, implying $\alpha \simeq 0.15$ and $x \simeq 0.4$. This scenario prescribes that the heat flux decreases with depth across the mixing layer $\phi_\chi \propto |z|^{-0.15}$. On the other hand, Fig. 4 could possibly reflect constant behaviour $Nu \propto t^0$—only polluted by finite-size effects. This constant-flux scenario implies $\alpha = 0$ and $x \simeq 0.25$. Both scenarios can be examined directly. To compute the universal profiles Θ, Φ_θ, etc, we suppress the fluctuations in Eq. (3.6) by first rescaling $z \to z/L(t)$, multiplying by the suitable power of L and then temporally averaging. The results are shown in Fig. 7. Inspection of the thermal flux supports the exponent $\alpha = 0$, corresponding to an approximately constant flux across the domain and implying the scaling $\eta^{-0.25}$ for thermal layer away from the front. The solutal layer is rather characterised by the exponents $\alpha \simeq 0.15$ and $x \simeq 0.4$. The difference between thermal and solutal similarity may reflect the asymmetric roles of temperature and salinity, which respectively provide destabilising and stabilising contributions to the initial density profile.

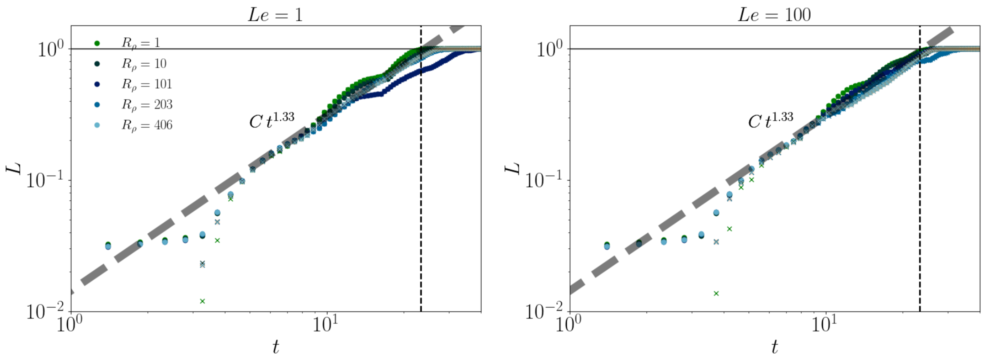

Figure 8: Left: Time evolution of the thermal (o) and solutal (x) mixing lengths at $Le = 1$ for various density ratios. The vertical dashed line marks the time at which the fronts reach the bottom boundary. Right: Same but for $Le = 100$.

3.4. *Universality of the convective regime*

The convective regime is largely insensitive to variations of the density ratio and the Lewis number. To provide a systematic estimate of the convective mixing layer, we compute $L(t)$ by thresholding the heat flux at a small cutoff value $\epsilon = 10^{-12}$, explicitly defining

$$L(t) = \sup\left\{|z|, \phi_\theta(t) \geqslant 10^{-12}\right\}. \tag{3.11}$$

Figure 8 gathers the data, revealing the universality of the superdiffusive rate (3.4) across the range of Le and R_ρ investigated. This universality is compatible with the similarity scenario sketched in § 3.3: the mixing layer growth is driven by a constant-flux similarity solution, associated to the inviscid dynamics within the bulk. The latter is obtained by formally setting $Re \to \infty$ in (2.3). This scenario explains why the constant C_f measured in Fig. 4 is independent both from Le and R_ρ.

Double-diffusive effects are present only close to the upper interface. They regulate the exchanges between the boundary meltwater layer and the turbulent mixing layer. We quantify these exchanges through the efficiency ratios

$$\Gamma_\chi(t) = \frac{|\Phi^c_\chi(\eta = 0.5)|}{|\phi^d_\chi(z = 0)|}, \quad \chi \equiv \theta, \sigma, \tag{3.12}$$

estimating the relative strength of the convective flux—estimated halfway towards the front—compared with the diffusive flux at the interface. Figure 9 shows the result at a time $t = 10$, when the turbulent layer is developed but occupies only $1/5$ of the box—still far from the bottom boundary. For the thermal fluxes, the efficiency ratio $\simeq 1.8$ is largely independent of the density ratio and Lewis number. A transition at $R_\rho \lesssim 10$ between relatively saline and relatively fresh environments is apparent for the solutal efficiency. For a fixed Lewis, the solutal efficienty varies midly in the fresh case, $R_\rho \lesssim 10$, and decreases algebraically $\propto R_\rho^{-1}$ in the salty case, $R_\rho \gtrsim 10$. This transition is compatible with that observed in Fig. 4 for the time evolution of the Nusselt number, marking the onset of the regime of diffusive decay $Nu \propto t^{-0.5}$ and the formation of the (fresh) diffusive boundary layer near the top interface. This layer does not impact the statistics of turbulent mixing within the bulk, but regulates the amount of salt deficit injected into it. The efficiency decreases with Lewis; Asymptotic estimates relying on the diffusive nature of the boundary layer dynamics predict $\propto Le^{-1} R_\rho^{-1}$. Such estimates are obtained from the diffusive phenomenology described in Appendix B—

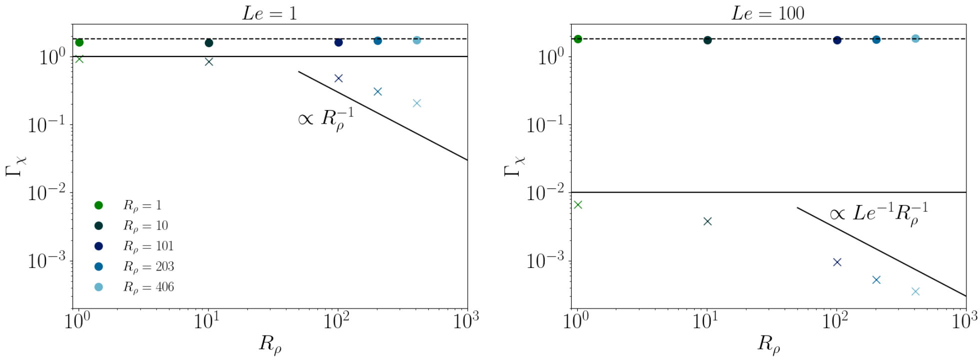

Figure 9: Thermal flux ratio Γ_θ (circles) and solutal flux ratio Γ_σ (crosses) for different density ratios. Left: $Le = 1$. Right: $Le = 100$. The horizontal lines indicate $\Gamma_\theta = 1.8$ (dashed) and $\Gamma_\sigma = Le^{-1}$ (solid). The indicative scalings $\propto Le^{-1}R_\rho^{-1}$ share a common prefactor $\simeq 30$.

in particular the gradient estimate (B 3) $\partial_z\sigma \propto \sigma_0 Le^{1/2}/\sqrt{t}$ and the scaling estimate (B 5) $\sigma_0 \propto R_\rho Le^{1/2}$. This scaling law is shown in Fig. 9 and is compatible with our observations. It implies that only a small fraction $\propto Le^{-1}R_\rho^{-1}$ of the input solutal flux permeates through the interfacial layer to reach the convective layer.

3.5. *Comments on mixing lengths*

At high R_ρ, the physics involves an interplay between turbulent and diffusive flows, making the interpretation of mixing lengths strongly dependent on their practical evaluation. The mixing length $L(t)$ used in the previous section tracks the turbulent front, and is hence unaffected by the fresh boundary layer. It emphasises the role of thermally-induced convection and is largely independent of Le and double-diffusive effects within the bulk.

Among various options, the temperature and salinity mixing layers could be defined from different threshold values on the scalar fields themselves, as illustrated in Fig. 10. We observe that the temperature mixing layer exhibits the universal super-diffusive growth $Ct^{1.33}$ prescribed by Eq. (3.4) regardless of the selected threshold. In contrast, the solutal mixing layer exhibits a strong dependence on the chosen threshold. For small thresholds, the definition captures the turbulent front, and the growth remains as $Ct^{1.33}$. Increasing the threshold, the mixing length captures the near-interfacial dynamics, driven by the fresh, stably stratified meltwater layer. In this case, the solutal mixing length grows diffusively as $L_\sigma \sim D_\sigma t^{1/2}$, with a prefactor D_σ that depends on the threshold value.

These results highlight the sensitivity of mixing diagnostics to their precise definition. Here, different thresholds probe distinct physical processes, from turbulent transport in the bulk to diffusion-dominated dynamics near the interface. This sensitivity suggests potential caveats in more complex oceanographic settings, where mixed-layer depths are commonly defined using scalar threshold-based criteria (de Boyer Montégut 2024; Allende *et al.* 2023).

4. Concluding remarks

We have examined the melt-driven convection beneath an ice–ocean interface. Consistent with previous studies (Xue *et al.* 2024), our setting exhibits a subdiffusive-dominated regime $\propto t^{-0.2}$ at small R_ρ and a diffusion-dominated regime $\propto t^{-0.5}$ at large R_ρ in the regulation of the thermal flux at the upper boundary. However, we find that the diffusive dynamics remain

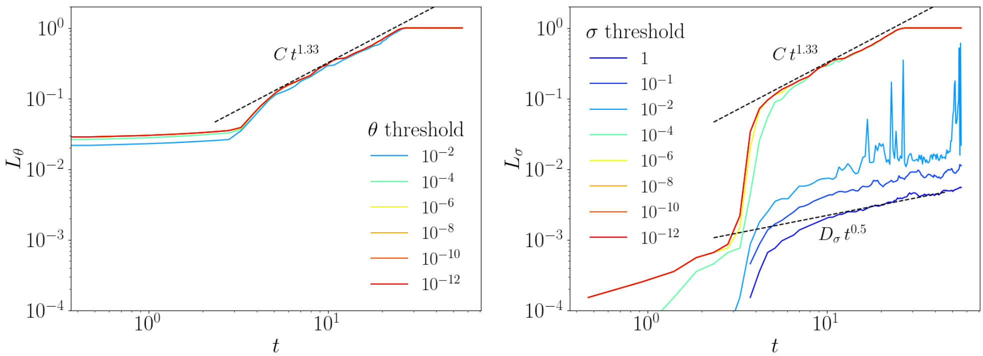

Figure 10: Temporal evolution of the mixing length evaluated at Le = 100 and R_ρ = 406 using different thresholds. Left: Thermal mixing length. Left: solutal mixing length.

confined only to a thin interfacial layer, with the bulk flow evolving through a (turbulent) convective thermal layer. Regardless of the near-interface regime, the front of the turbulent layer grows super-diffusively as $L \propto t^{4/3}$ for all R_ρ and Le. This scaling differs from the t^2 growth associated with Rayleigh–Taylor convection (Chertkov 2003; Boffetta & Mazzino 2017), reflecting the presence of a rigid lid at the top boundary. The melting boundary condition controls the solutal flux in the convective mixing layer. In particular, for large density ratios, only a fraction $\propto R_\rho^{-1}$ of the meltwater input flux contributes to the solutal convective flux in the bulk.

While strongly idealised, our setting showcases a non-trivial interplay between a diffusive meltwater boundary layer and a convective interior. The interfacial layer is governed by double-diffusive effects, while turbulent transport drives the bulk. The simplicity of the setting, which represents meltwater input as a nonlinear boundary condition without explicitly resolving phase transitions, allows to decipher the governing scaling laws. In short, the physics related to the interfacial boundary layer exhibits strong dependence on Le and R_ρ, while that related to convective effects is largely universal. Our simulations suggest a constant-flux scenario across the turbulent mixing layer, implying in particular that the subdiffusive evolution of Nusselt at the boundary $\propto t^{-0.2}$ is a finite-Reynolds effect, likely reflective of an asymptotic regime characterised by a constant-Nusselt meltwater input.

Several questions remain relating to the detailed phenomenology of the flow and its dependence upon key physical parameters (dimensionality, initial stratifications, non-stationarity). Achieving a detailed phenomenology of melting-driven turbulence, in the spirit of the work of Chertkov (2003) on Rayleigh-Taylor turbulence constitutes a natural theoretical extension of the present work. Another issue relates to the flow universality, as the sharp interfacial gradient at the top interface makes the initial configuration effectively singular, with potential implications for its statistical predictability—see, *e.g.* (Biferale *et al.* 2018; Thalabard *et al.* 2020). To control the regularisation of the initial singularity, we chose to initiate melting through a thermal Rayleigh–Taylor instability slightly offset from the interface. This physical regularisation enables the boundary conditions to be explicitly enforced at early times, and triggers the convective turbulent layer. While no dependence on $\delta \to 0$, was found, it remains unclear whether such turbulent generation is universal across different regularisation schemes—in particular implementations relying on implicit regularisations only through numerical discretisation.

Acknowledgements

SA was supported by the Marie Sk lodowska-Curie Actions (MSCA) under grant agreement 101150225. This work was granted access to the HPC resources of TGCC under the GENCI allocation A0170115703 (project: Simulation Numérique des Interactions entre l'Océan et la Glace de Mer).

REFERENCES

Allende, S, Fichefet, T., Goosse, H. & Treguier, A-M. 2023 On the ability of OMIP models to simulate the ocean mixed layer depth and its seasonal cycle in the arctic ocean. *Ocean Modelling* **184**, 102226.

Allende, S., Treguier, A.-M., Lique, C., de Boyer Montégut, C., Massonnet, F., Fichefet, T. & Barthélemy, A. 2024 Impact of ocean vertical-mixing parameterization on arctic sea ice and upper-ocean properties using the NEMO-SI3 model. *Geoscientific Model Development* **17** (20), 7445–7466.

Barenblatt, G. 1996 *Scaling, self-similarity, and intermediate asymptotics: dimensional analysis and intermediate asymptotics*. Cambridge University Press.

Berhanu, M., Philippi, J., Courrech du Pont, S. & Derr, J. 2021 Solutal convection instability caused by dissolution. *Physics of Fluids* **33** (7).

Biferale, L., Boffetta, G., Mailybaev, A. & Scagliarini, A. 2018 Rayleigh-Taylor turbulence with singular nonuniform initial conditions. *Physical Review Fluids* **3** (9), 092601.

Boffetta, G. & Mazzino, A. 2017 Incompressible Rayleigh–Taylor turbulence. *Annual Review of Fluid Mechanics* **49** (1), 119–143.

de Boyer Montégut, C 2024 Mixed layer depth over the global ocean. *SEANOE [data set]* **10**, 98226.

Campolina, C., Simonnet, E. & Thalabard, S. 2025 Non-unique self-similar blowups in shell models: insights from dynamical systems and machine-learning. *Journal of Physics A: Mathematical and Theoretical* **58** (17), 175701.

Chertkov, M. 2003 Phenomenology of Rayleigh-Taylor turbulence. *Physical Review Letters* **91** (11), 115001.

Cohen, C., Berhanu, M., Derr, J. & Courrech du Pont, S. 2020 Buoyancy-driven dissolution of inclined blocks: Erosion rate and pattern formation. *Physical Review Fluids* **5** (5), 053802.

Couston, L.-A. 2024 Turbulent ice-ocean boundary layers in the well-mixed regime: insights from direct numerical simulations. *Journal of Physical Oceanography* .

Drazin, P. & Reid, William H. 2004 *Hydrodynamic stability*. Cambridge university press.

Du, Y., Calzavarini, E. & Sun, C. 2024 The physics of freezing and melting in the presence of flows. *Nature Reviews Physics* **6** (11), 676–690.

Favier, B., Purseed, J. & Duchemin, L. 2019 Rayleigh–Bénard convection with a melting boundary. *Journal of Fluid Mechanics* **858**, 437–473.

Gastine, T. & Favier, B. 2025 Rotating convection with a melting boundary: An application to the icy moons. *Icarus* **429**, 116441.

Gayen, B., Griffiths, R. & Kerr, R. 2016 Simulation of convection at a vertical ice face dissolving into saline water. *Journal of Fluid Mechanics* **798**, 284–298.

Guo, R. & Yang, Y. 2025 The effects of double diffusive convection on the basal melting of solid ice in seawater. *Journal of Fluid Mechanics* **1013**, A24.

Hewitt, I. 2020 Subglacial plumes. *Annual Review of Fluid Mechanics* **52** (1), 145–169.

Huppert, H. 1990 The fluid mechanics of solidification. *Journal of Fluid Mechanics* **212**, 209–240.

Jenkins, A. 1999 The impact of melting ice on ocean waters. *Journal of physical oceanography* **29** (9), 2370–2381.

Keitzl, T., Mellado, J.-P. & Notz, D. 2016 Impact of thermally driven turbulence on the bottom melting of ice. *Journal of Physical Oceanography* **46** (4), 1171–1187.

Middleton, L., Vreugdenhil, C., Holland, P. & Taylor, J. 2021 Numerical simulations of melt-driven double-diffusive fluxes in a turbulent boundary layer beneath an ice shelf. *Journal of Physical Oceanography* **51** (2), 403–418.

Millero, Frank J 2010 History of the equation of state of seawater. *Oceanography* **23** (3), 18–33.

Peralta-Ferriz, C. & Woodgate, R. 2015 Seasonal and interannual variability of pan-Arctic surface mixed layer properties from 1979 to 2012 from hydrographic data, and the dominance of stratification for multiyear mixed layer depth shoaling. *Progress in Oceanography* **134**, 19–53.

Ramadhan, A., Wagner, G., Hill, C., Campin, J.-M., Churavy, V., Besard, T., Souza, A., Edelman, A., Ferrari, R. & Marshall, J. 2020 Oceananigans. jl: Fast and friendly geophysical fluid dynamics on GPUs. *Journal of Open Source Software* **5** (53).

Rosevear, M.G., Gayen, B., Vreugdenhil, C.A. & Galton-Fenzi, B.K. 2025 How does the ocean melt antarctic ice shelves? *Annual Review of Marine Science* **17**.

Talley, Lynne D 2011 *Descriptive physical oceanography: an introduction*. Academic press.

Thalabard, S., Bec, J. & Mailybaev, A. A. 2020 From the butterfly effect to spontaneous stochasticity in singular shear flows. *Communications Physics* **3** (1), 122.

Vreugdenhil, C. & Taylor, J. 2019 Stratification effects in the turbulent boundary layer beneath a melting ice shelf: Insights from resolved large-eddy simulations. *Journal of Physical Oceanography* **49** (7), 1905–1925.

Wettlaufer, J. 2001 The Stefan problem: Polar exploration and the mathematics of moving boundaries. *Die Zentralanstalt für Meteorologie und Geodynamik, 1851–2001, 150 Jahre Meteorologie und Geophysik in Osterreich* pp. 420–435.

Xu, Dehao, Yang, Rui, Verzicco, Roberto & Lohse, Detlef 2025 Aspect ratio effect on side and basal melting in fresh water. *Journal of Fluid Mechanics* **1010**, A40.

Xue, Z.-H., Zhang, J. & Ni, M.-J. 2024 Flow regimes in a melting system composed of binary fluid: transition from penetrative convection to diffusion. *Journal of Fluid Mechanics* **998**, A14.

Yang, R., Howland, C., Liu, H.-R., Verzicco, R. & Lohse, D. 2023 Ice melting in salty water: layering and non-monotonic dependence on the mean salinity. *Journal of Fluid Mechanics* **969**, R2.

Yang, R., Xu, D., Verzicco, R. & Lohse, D. 2025 Asymmetric equilibrium states for melting and freezing in thermal convection. *Journal of Fluid Mechanics* **1017**, A12.

Appendix A. Details on the numerical protocol

This section provides additional information regarding our numerical protocol, detailing the initial conditions and the role of δ as a smoothing numerical parameter.

A.1. *Initial conditions*

The initial salinity field is taken to be spatially uniform, $S_i(x,z) = S_\infty$. This choice prescribes both the interfacial temperature at the ice–water boundary through the freezing-point relation and the far-field temperature as, respectively,

$$T_{\text{top}} = T_m(S_\infty) := T_{\text{f},0} + \lambda_1 S_\infty, \qquad T_\infty = T_{\text{top}} + \Delta T. \tag{A 1}$$

In order to avoid an abrupt numerical adjustment at the interface, we smooth out the temperature jump over a thin vertical layer of thickness δ. Specifically, we define $z_0 = -2\delta$, $h = \delta/4$ to construct the (unperturbed) background temperature profile as

$$T_i(z) = \frac{T_\infty + T_{\text{top}} \exp\left(2\frac{z-z_0}{h}\right)}{1 + \exp\left(2\frac{z-z_0}{h}\right)}, \tag{A 2}$$

which interpolates between $T_i(-\infty) = T_\infty$ and $T_i(0) = \left(T_\infty e^{-16} + T_{top}\right)/(e^{-16} + 1) \simeq T_{top}$. This temperature field has a vanishing gradient at the top interface and therefore satisfies the boundary condition (2.5) with the constant field $S_i(x,z) = S_\infty$. To seed instabilities, the temperature field is perturbed by small-amplitude Gaussian random noise, drawn independently and everywhere in space as

$$T_i^\epsilon(x,z) = T_i(z) + \sqrt{\epsilon}\eta(x,z) \quad \eta(x,z) \sim \mathcal{N}(0,1)\,.$$

In our simulations, we typically set $\epsilon = 10^{-10}$ and $\delta = 0.05\,L_z$.

A.2. *Numerical implementation of the boundary conditions*

At the ice–ocean interface, the dimensional version of the melting boundary conditions (2.5) involve the top salinity $S_{\text{top}} = S(z=0)$ and the temperature $T_{\text{top}} = T(z=0)$, together with their derivatives as

$$T_{\text{top}} = T_m(S_{\text{top}}) \text{ (melting point)} \quad \text{and} \quad \left.\frac{\partial S}{\partial z}\right|_{z=0} = Le^{-1} S_{\text{top}} \frac{St}{\Delta T} \left.\frac{\partial T}{\partial z}\right|_{z=0} \text{ (flux balance)}, \tag{A 3}$$

where we recall that Le, St and ΔT denote the Lewis number, the Stefan number and the temperature jump, respectively. The melting point $T_M(S) = T_{\text{f},0} + \lambda_1 S$ is a function of salinity with the empirical coefficients $\lambda_1 = -5.73 \times 10^{-2}$ K/(g/kg), and $T_{f,0} = 273.15K$.

To enforce the boundary condition A 3 in our numerics, we discretise it with finite-difference scheme in order to prescribe at each time step a value for T_{top} and S_{top} as a function of T_1 and S_1—representing the temperature and salinity at gridpoints $z = -\Delta z$. Substituting the flux balance into the melting condition yields a quadratic equation for the interfacial temperature:

$$T_{\text{top}}^2 + bT_{\text{top}} - c = 0, \quad \text{with} \quad \begin{cases} b(T_1, S_1) := T_1 + \dfrac{1}{Le}\dfrac{\Delta T}{St} + T_{\text{f},0}, \\ c(T_1, S_1) := \dfrac{1}{Le}\dfrac{\Delta T}{St}\lambda_1 S_1 + T_{\text{f},0}\left(T_1 + \dfrac{1}{Le}\dfrac{\Delta T}{St}\right). \end{cases} \tag{A 4}$$

The physically relevant root is the one prescribing the positive interfacial temperature

$$T_{\text{top}} = \frac{-b + \sqrt{b^2 + 4c}}{2}, \tag{A 5}$$

which in turn prescribes the interfacial salinity

$$S_{\text{top}} = \frac{T_{\text{top}} - T_{\text{f},0}}{\lambda_1}. \tag{A 6}$$

Appendix B. Diffusive dynamics near the boundary

In our setting, the melting boundary at the top requires vanishing normal flow. The dynamics of the temperature and the salinity therefore reduce to the diffusive dynamics

$$\partial_t \theta = Re^{-1}\, Pr^{-1} \Delta\theta, \quad \partial_t \sigma = Re^{-1}\, Pr^{-1}\, Le^{-1} \Delta\sigma, \tag{B 1}$$

Figure 5 suggests that at $t \gtrapprox 5$, both the temperature and the salinity reach interfacial values that only slowly vary in time. Treating those values as stationary with respect to diffusive processes and averaging over x yields explicit solution in terms of the interfacial values:

$$\langle\theta\rangle_x = (\theta_0 - 1)\ \text{erfc}\left(\frac{|z|}{\delta_\theta}\right), \quad \langle\sigma\rangle_x = \sigma_0\, \text{erfc}\left(\frac{|z|}{\delta_\sigma}\right), \tag{B 2}$$

where $\delta_\theta(t) := Re^{-1/2} Pr^{-1/2} t^{1/2}$ and $\delta_\sigma(t) := Le^{-1/2}\delta_\theta$. We use the complementary error function $\text{erfc}(z) = \frac{2}{\sqrt{\pi}} \int_z^\infty e^{-u^2/2} du$ and recall the shorthand $\sigma_0 = \langle\sigma\rangle_{x,z=0}$ and $\theta_0 = \langle\theta\rangle_{x,z=0} + 1$— denoting the excess temperature. Equation (B 2) provides the gradient estimates at the interface as

$$\partial_z \langle\theta\rangle_x|_{z=0} = \frac{2}{\sqrt{\pi}} \frac{\theta_0 - 1}{\delta_\theta}, \quad \partial_z \langle\sigma\rangle_x|_{z=0} = \frac{2}{\sqrt{\pi}} \frac{\sigma_0}{\delta_\sigma}. \tag{B 3}$$

Substituting those estimates into the melting condition in Eq. (2.5) yields

$$\theta_0 = -\gamma_1\sigma_0, \quad \sigma_0 = -\left(\sigma_0 + R_\rho\right) Le^{1/2}\, St\,(\gamma_1\sigma_0 + 1)\,. \tag{B 4}$$

For small solutal perturbations such that $\sigma_0 \ll R_\rho$ and $\sigma_0 \ll \gamma_1^{-1}$, this yields the scaling estimate

$$\theta_0 = -\gamma_1 \sigma_0 \sim St Le^{1/2} R_\rho \quad ; \tag{B 5}$$

This is compatible with the scaling $O(Le^{1/2} R_\rho)$ observed in Fig. 5.

Combined with Eq. (B 3), this yields the following (diffusive) estimate for the Nusselt number

$$Nu = C_s t^{-1/2}, \quad C_s \simeq \frac{2}{\sqrt{\pi}} (RePr)^{1/2} \left(1 - Le^{1/2} St R_\rho\right). \tag{B 6}$$

The estimate support the dispersive nature of the diffusive constant C_s, with respect to the Lewis number Le and the density ratio R_ρ seen in Fig. 4. Quantitatively, it does capture the decrease of C_s with R_ρ observed in panels (a,b) of Fig. 4. It however fails to reflect the small increase with Le at high R_ρ, and does not yield the specific scaling exponents in the transitional region between diffusive and convective regimes. Capturing this effect would require a refined asymptotic analysis involving higher-order corrections.